Optics Letters

Orbital angular momentum bistability in a microlaser

N. Carlon Zambon,[1,†] P. St-Jean,[1,†,*] A. Lemaître,[1] A. Harouri,[1] L. Le Gratiet,[1] I. Sagnes,[1] S. Ravets,[1] A. Amo,[2] and J. Bloch[1]

[1]Centre de Nanosciences et de Nanotechnologies (C2N), CNRS—Université Paris-Sud/Paris-Saclay, Palaiseau, France
[2]Université de Lille, CNRS, UMR 8523 PhLAM—Physique des Lasers Atomes et Molécules, F-59000 Lille, France
*Corresponding author: philippe.st-jean@c2n.upsaclay.fr

Received 7 May 2019; revised 18 June 2019; accepted 7 August 2019; posted 12 August 2019 (Doc. ID 366418); published 11 September 2019

Light's orbital angular momentum (OAM) is an unbounded degree of freedom emerging in helical beams that appears very advantageous technologically. Using chiral microlasers, i.e., integrated devices that allow generating an emission carrying a net OAM, we demonstrate a regime of bistability involving two modes presenting distinct OAM ($\ell = 0$ and $\ell = 2$). Furthermore, thanks to an engineered spin-orbit coupling of light in these devices, these modes also exhibit distinct polarization patterns, i.e., circular and azimuthal polarizations. Using a dynamical model of rate equations, we show that this bistability arises from polarization-dependent saturation of the gain medium. Such a bistable regime appears very promising for implementing ultrafast optical switches based on the OAM of light. As well, it paves the way for the exploration of dynamical processes involving phase and polarization vortices.

https://doi.org/10.1364/OL.44.004531

Electromagnetic waves carry angular momentum through two main contributions: spin angular momentum associated to circular polarization, and orbital angular momentum (OAM) emerging in beams presenting a helical phase front [1]. While the former is restricted to $\pm\hbar$, OAM is theoretically unbounded, as it can take any value $\ell\hbar$, where ℓ is an integer corresponding to the number of times the phase front winds around the propagation axis within an optical period.

Such an unbounded degree of freedom of light appears very advantageous technologically. Indeed, transferring arbitrarily large values of angular momentum to massive objects is a powerful asset in opto-mechanics [2] and for optical trapping schemes [3]. Moreover, it could allow multiplexing classical [4] or quantum information [5,6] in higher-dimensional bases, thus enhancing the density and robustness of transmission channels.

Fully taking profit of such high-dimensional bases requires the ability to manipulate OAM-carrying beams not only with linear optical elements, but also in the nonlinear regime. The most notable demonstrations of nonlinear optical control of the OAM include the generation of higher harmonics in nonlinear crystals [7] and atomic vapors [8], of OAM-entangled photon pairs by parametric downconversion [9], and the observation of optical bistability involving a single OAM mode [10]. Furthermore, a recent demonstration of OAM microlasers [11] where the chirality of the emission can be optically controlled from clockwise to counter-clockwise vortices [12] offers new opportunities for exploring OAM-based nonlinear optics in integrated devices.

In this Letter, we experimentally show that nonlinear effects associated to gain saturation in such microlasers lead to an optical bistability between modes presenting distinct values of OAM (i.e., $\ell = 0$ and $+2$). Moreover, an engineered spin-orbit coupling of light in these devices allows switching not only the OAM magnitude of the beam, but also its polarization texture, from circularly to azimuthally polarized. This confluence of optical bistability and spin-orbit coupling of light are particularly interesting, as they open the door to the exploration of dynamical processes (e.g., quenches and phase transitions) involving distinct phase and polarization vortices [13].

The chiral microlasers used in this Letter are built from semiconductor microcavities grown by molecular beam epitaxy. The cavities consist of a GaAs layer embedding a single 17 nm $In_{0.04}Ga_{0.96}As$ quantum well and inserted between two $Al_{0.95}Ga_{0.05}As/Al_{0.10}Ga_{0.90}As$ Bragg mirrors formed from 32 (36) pairs in the top (bottom); the measured quality factor of the cavity is $Q \approx 4 \cdot 10^4$. To obtain microlasers with the appropriate discrete rotational symmetry for generating OAM, the cavities are processed by electron beam lithography and dry etching techniques to form hexagonal rings of coupled micropillars. Figure 1(a) shows an electron microscopy image of the specific device used in this Letter. (The pillar diameter is 3.2 μm, and the inter-pillar distance is 2.4 μm.)

Due to the discrete rotational symmetry of the microstructure, the photonic eigenmodes can be classified by their angular momentum ℓ, associated to the evolution of the phase around the device [12,14]. In the tight-binding limit, this leads to the following four energy levels characterized by the quantum numbers $\ell = 0, \pm 1, \pm 2, 3$:

$$|\ell\rangle = \frac{1}{\sqrt{6}} \sum_j e^{2\pi i \ell j/6} |\phi_j\rangle, \tag{1}$$

where $|\phi_j\rangle$ corresponds to the ground state of the jth pillar.

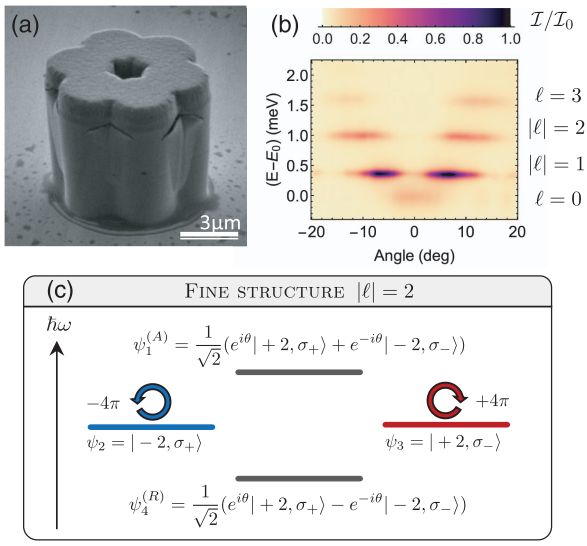

Fig. 1. (a) SEM image of a device. (b) Angle-resolved emission spectrum of the molecule exhibits four energy levels corresponding to angular momenta $\ell = 0, \pm 1, \pm 2$ and 3. (c) Fine structure of the $|\ell| = 2$ manifold in the presence of spin-orbit coupling. The middle states present a net OAM $\ell = \pm 2$ and opposite polarizations: σ_+ (blue) and σ_- (red).

States $|\ell = 0\rangle$ and $|\ell = 3\rangle$ do not carry angular momentum as their wave-function evolves, respectively, in- and out-of-phase between neighboring pillars. On the other hand, states $|\ell = \pm 1\rangle$ and $|\ell = \pm 2\rangle$ carry a net angular momentum, corresponding to phase vortices of $\pm 2\pi$ and $\pm 4\pi$. These four energy levels are observed, well below the lasing threshold, with angle- and energy-resolved photoluminescence measurements [Fig. 1(b)].

In order to generate a chiral emission, we take profit of the coupling between the spin and orbital angular momenta of photons that emerges in dielectric microcavities [14–16]. This spin-orbit effect arises from an anisotropic inter-pillar coupling: the coupling energy is greater for photons polarized parallel to the axis linking two neighboring pillars than for photons polarized perpendicularly [17]. As a result of this azimuthally varying birefringence axis, the degeneracy of $\ell = \pm 1$ and $\ell = \pm 2$ manifolds is lifted resulting in three-level fine structures. ($\ell = 0$ and $\ell = 3$ manifolds are not affected by this spin-orbit effect, as they do not carry OAM.) These fine structures cannot be spectrally resolved below the lasing threshold [Fig. 1(b)], because the linewidth is larger than the energy spacing (related to the hopping anisotropy of ∼20 μeV); however, it can be accessed in the lasing regime where the emission lines narrow significantly [12,14].

For the specific case of the $|\ell| = 2$ manifold which will be of particular interest in this Letter, the fine structure is presented in Fig. 1(c). The highest (ψ_1) and lowest (ψ_4) energy levels correspond to the linear combinations of $\pm 4\pi$ phase vortices, each associated to orthogonal circular polarizations ($\sigma_\mp$). Therefore, these states do not carry a net OAM (i.e., the expectation value of ℓ is 0) and are linearly polarized, either azimuthally (ψ_1) or radially (ψ_4). The middle states ($\psi_{2,3}$) do carry a net angular momentum ($\ell = \pm 2$) and exhibit opposite circular polarizations. Thanks to the relatively slow spin relaxation time of photogenerated electrons in $In_xGa_{1-x}As$ semiconductor quantum wells, it is possible to spin-polarize the gain medium with a circularly polarized off-resonant pump [12,18]. This polarized gain medium gives rise to a higher gain for the mode polarized accordingly to the pump. In this Letter, we show the emergence of a bistable regime involving states ψ_1 and ψ_2 of this fine structure.

The device investigated presents a geometry such that the gain/loss ratio is maximal for the $|\ell| = 2$ manifold, with an emission energy $E \sim 1.47$ eV (see Ref. [12] for details on this lasing scheme). All measurements were done at $T = 4K$. The evolution of the emission intensity as a function of pumping power [Fig. 2(a)] shows a lasing threshold around $P_{th} \sim 0.35$ kW/cm^2 and a saturation regime around 0.75 kW/cm^2. In such a cavity, lasing occurs in the weak coupling regime so that no polariton physics is involved above threshold [19]. Under a σ_+-polarized off-resonant CW pump ($E_{pump} = 1.6$ eV), lasing occurs in mode ψ_2 which carries an OAM of $\ell = +2$. This is evidenced by doing a self-interferometry measurement of the beam [Fig. 2(b)] which reveals a double pitchfork in the fringe pattern; in addition, the extracted phase map exhibits a 4π phase vortex [Fig. 2(c)].

Upon increasing the incident power of a σ_+-polarized pump far above the lasing threshold, the competition between these two modes ($\psi_{1,2}$) leads to the emergence of a bistable regime without intensity jumps. A hysteresis cycle is clearly seen in Fig. 3(a), where we present the emission energy as a function of pump power. The power range of the plot corresponds to the yellow area in Fig. 2(a). The black (red) dots are measured when the power is ramped up (down). When ramping up the excitation power, the emission energy exhibits an abrupt jump ($\Delta E_{12} \sim 20$ μeV) around $P = 5.5P_{th}$(1.85 kW/cm^2). This jump is accompanied by a drastic change in the spatial profile of the beam: under horizontal polarization filtering, the profile switches from a homogeneous doughnut shape (upper-left inset) to a four-lobe profile (lower-right inset). Throughout this bistability region, the emission remains strongly single mode with a sideband suppression of more than 25 dB. [Figures 3(b) and 3(c), respectively, present emission spectra measured below and above the bistability.] Both this shift of energy and change of the spatial profile indicate a mode switch toward the highest energy mode ψ_1 at high excitation powers.

Upon decreasing the excitation power [red dots in Fig. 3(a)], we observe an abrupt lowering of the emission energy around $P = 4P_{th}$(1.3 kW/cm^2) back to its initial value (i.e., that in

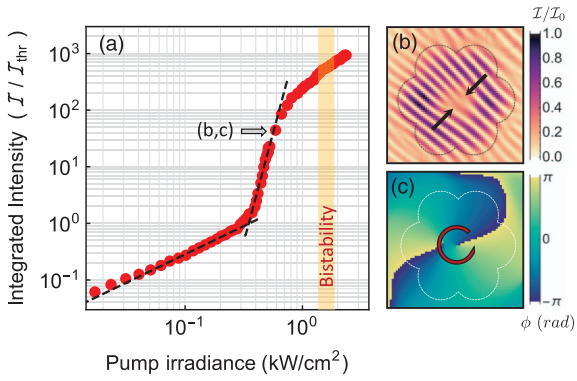

Fig. 2. (a) Integrated emission intensity as a function of pump power density. The yellow area indicates the bistability region. (b) Self-interference pattern and (c) and extracted phase map of the beam under a σ_+ polarized pump.

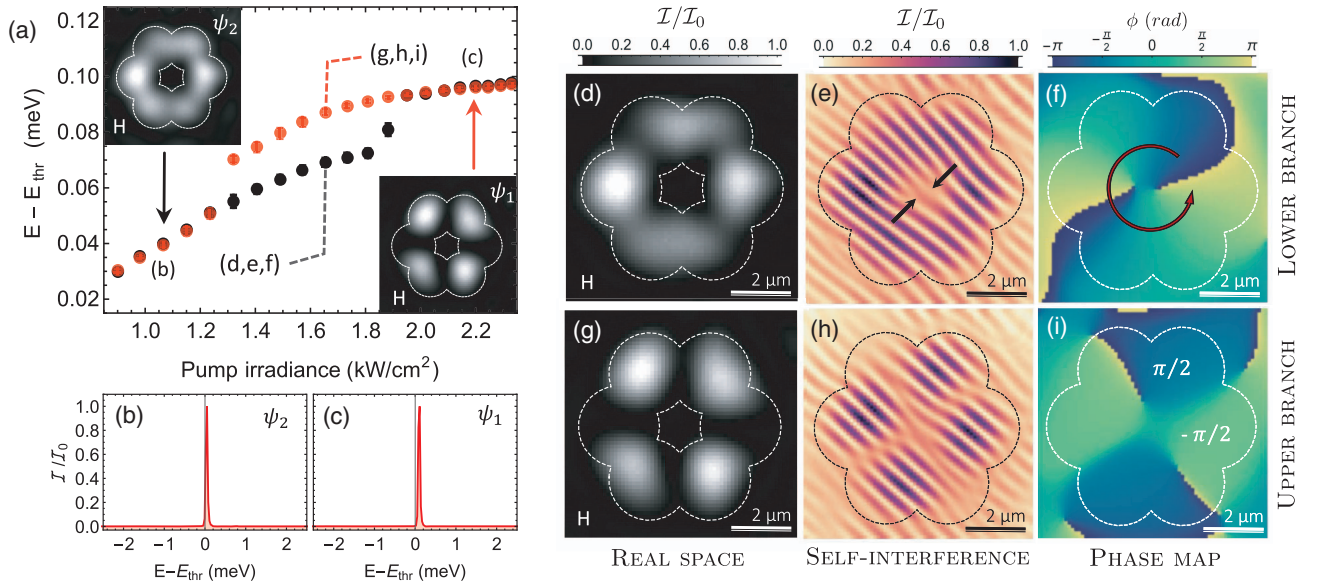

Fig. 3. (a) Emission energy as a function of excitation power, when the power is ramped up (black dots) and down (red dots). The insets the show real space images of the beam below and above the bistability. Emission spectra (b) below and (c) above the bistability. (d), (g) Real space images; (e), (h) self-interferometry patterns; and (f), (i) corresponding phase maps measured in the (d)–(f) lower and (g)–(i) upper branches of the bistability, at the same pump power. All images are taken with a horizontal polarization filtering.

the upward scan). This jump is also accompanied by an abrupt change in the spatial pattern, back to its homogeneous shape. Thus, we evidence a hysteretic cycle that indicates a region of bistability involving two states presenting distinct OAM, i.e., $\ell = 0$ (ψ_1) and $\ell = +2$ (ψ_2), and distinct polarization textures, i.e., circular (ψ_2) and azimuthal (ψ_1) polarizations.

To evidence this bistable regime more clearly, we present images of the beam at an intermediate pump power of $P = 4.7P_{\text{th}}(1.65\ \text{kW/cm}^2)$. Figure 3 presents spatial profiles of the beam (d), (g), interferograms (e), (h) and corresponding phase maps (f), (i), measured, respectively, in the lower (d)–(f) and upper (g)–(i) branches of the hysteresis cycle. This allows further identifying modes involved in the bistability through their polarization and phase patterns [14]. Indeed, real space images (with horizontal polarization filtering) in the upper and lower branches show, respectively, the four-lobe and homogeneous patterns characteristic of ψ_1 and ψ_2. Furthermore, fringe patterns measured in the lower branch show two pitchforks as expected for a mode carrying an OAM of $\ell = +2$, and the extracted phase map presents a 4π phase vortex. When measured in the upper branch, the phase map presents four abrupt jumps between $+\pi/2$ and $-\pi/2$. Such a phase profile describes well the standing wave that characterizes ψ_1 as a result of the linear combination of counter-propagating components $\ell = +2$ and $\ell = -2$: the phase jumps correspond to the nodes of this standing wave. Therefore, we clearly evidence abrupt switching between modes ψ_1 and ψ_2. Importantly, we want to point out that this bistable regime occurs at relatively low pump power as the gain medium consists of a single quantum well and, therefore, is not due to heating effects in the microstructure. Indeed, the abrupt jump in the upward scan is still observed when using a pulsed excitation with a duty cycle of 0.1% and a frequency of 1 kHz in order to mitigate thermal effects.

In order to describe phenomenologically the emergence of this bistable regime, we use a dynamical model involving rate equations for the time evolution of the two photonic modes ($\psi_{1,2}$) and two reservoir populations ($N_\uparrow$ and $N_\downarrow$), accounting, respectively, for spin-up and spin-down carriers. The system is described by the differential equations:

$$\begin{aligned}
\frac{dI_1}{dt} &= 0.5g_1(N_\uparrow + N_\downarrow)I_1 - \frac{I_1}{\tau_c} + 0.5\frac{N_\uparrow + N_\downarrow}{\tau_r},\\
\frac{dI_2}{dt} &= g_2 N_\uparrow I_2 - \frac{I_2}{\tau_c} + \frac{N_\uparrow}{\tau_r},\\
\frac{dN_\uparrow}{dt} &= P(1+\eta) - \left(0.5g_1 I_1 + g_2 I_2 + \frac{\beta}{\tau_r}\right)N_\uparrow,\\
\frac{dN_\downarrow}{dt} &= P(1-\eta) - \left(0.5g_1 I_1 + \frac{\beta}{\tau_r}\right)N_\downarrow.
\end{aligned} \tag{2}$$

Here $I_{1,2}$ is the photon number in modes $\psi_{1,2}$; $g_{1,2}$ are the gain coefficient of each mode; $\tau_c = 20$ ps is the photon lifetime; $\tau_r = 100$ ps is the carrier lifetime; β is the spontaneous emission factor; P is the pump power; and η is the degree of polarization of the gain medium extracted from the degree of polarization of the emission measured below the lasing threshold. Since both modes involved in the bistability belong to the same OAM manifold, we consider their non-radiative losses to be identical [12].

Bistable regimes have been extensively explored in bimodal lasers and are attributed to nonlinear contributions to the gain [20–22]. To account for such effects, we express the gain coefficients as $g_{1,2} = g_0(1 - \varepsilon_s^{(1,2)}I_{1,2} - \varepsilon_c^{(1,2)}I_{2,1})$, where g_0 is the unsaturated gain coefficient which is identical for $\psi_{1,2}$, and $\varepsilon_s^{(1,2)}$ and $\varepsilon_c^{(1,2)}$ are the self- and cross-saturation coefficients of $\psi_{1,2}$.

For two-mode lasers coupled to a single reservoir, the general requirement for bistability is $\varepsilon_s^{(1)}\varepsilon_s^{(2)} < \varepsilon_c^{(1)}\varepsilon_c^{(2)}$ [20–22]. Here the situation is slightly more complex, as the two modes couple

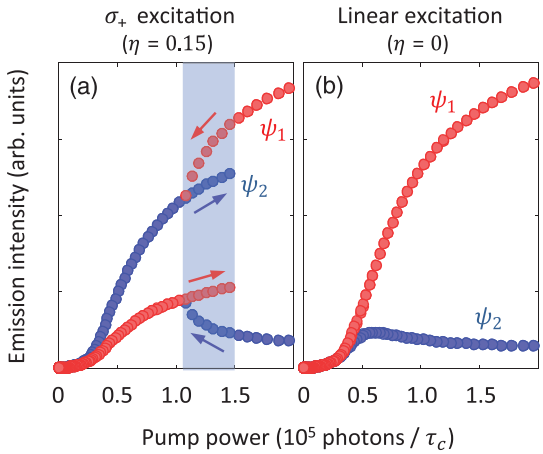

Fig. 4. Calculated intensity of the photonic modes ψ_1 and ψ_2 under a (a) circularly and (b) linearly polarized excitation. The blue area in Panel (a) corresponds to the bistability region, and the arrows indicated the scanning direction of the pump power. The coefficients used in both cases are the following: $g_0 = 11 \times 10^{-5}$ ps^{-1}, $\beta = 100$, $\varepsilon_s^{(1)} = \varepsilon_s^{(2)} = 5 \times 10^{-5}$, $\varepsilon_c^{(1)} = 5.43 \times 10^{-5}$, and $\varepsilon_c^{(2)} = 6 \times 10^{-5}$ ps^{-1}.

to two distinct reservoirs; moreover, due to their different polarization, they couple differently to each reservoir: ψ_1 (linearly polarized) couples identically to $N_\uparrow$ and $N_\downarrow$, whereas ψ_2 (circularly polarized) couples only to $N_\uparrow$. In order to account for the effect of this asymmetric coupling on the nonlinear dynamics of the system, we impose a second condition: $\varepsilon_c^{(1)} < \varepsilon_c^{(2)}$.

Figure 4(a) shows the adiabatic evolution of the computed intensity mode ψ_1 (red) and ψ_2 (blue); we clearly see the emergence of a bistable regime indicated by a blue rectangle. The coefficients (presented in the caption of Fig. 4) were defined in order to obtain a lasing threshold and bistability region at similar powers as those used experimentally. When changing the degree of polarization to $\eta = 0$ [Fig. 4(b)], thus simulating a linearly polarized pump, we do not observe any bistability, and the emission is now dominated by ψ_1. This is confirmed experimentally: under a linearly polarized excitation, lasing occurs in mode ψ_1 for the whole power range explored. Calculated relative intensities do not match the measured ones, as the minimalistic model we developed aims at providing a phenomenological understanding of the origin of the bistability, rather than a full description of the relative populations.

In conclusion, in this Letter, we showed how nonlinear effects in chiral microlasers can lead to a bistable regime involving modes with distinct OAM and polarization patterns. We further showed how dynamical rate equations can describe this process stemming from the confluence of co- and cross-saturation contributions to the gain. As the switching mechanism is expected to be limited by the relaxation of photo-generated carriers, it appears very interesting for implementing optical switches based on the OAM of light, as well as for exploring dynamical processes between phase and polarization vortices exhibiting distinct topological charges.

It is important to point out that such a bistability is not restricted to the specific values of OAM inspected in this Letter. Fabricating microlasers with n pillars (with n even and >4) could allow implementing similar fine structures as in Fig. 1(c) for $\ell = 1$ and $\ell = n/2 - 1$ [12]. This would lead to bistabilities involving modes with arbitrarily large values of OAM.

Funding. Honeypol, European Research Council (ERC); Quantum Fluids of Light, Agence Nationale de la Recherche (ANR-16-CE30-0021); PHOQUS, H2020 Future and Emerging Technologies (EU-FET); QUANTERA project Interpol, Agence Nationale de la Recherche (ANR-QUAN-0003-05); Labex CEMPI, Agence Nationale de la Recherche (ANR-11-LABX-0007); Labex NanoSaclay, Agence Nationale de la Recherche (ANR-10-LABX-0035); TOPOL, H2020 Marie Skłodowska-Curie Actions; French RENATECH network; CPER Photonics for Society P4S; TFLIGHT, Métropole Européenne de Lille; National Science and Engineering Research Council of Canada (NSERC).

Acknowledgment. The authors acknowledge insightful discussions with O. Bleu, G. Malpuech, and D. Solnyshkov.

†These authors contributed equally to this Letter.

REFERENCES

1. L. Allen, M. W. Beijersbergen, R. J. C. Spreeuw, and J. P. Woerdman, Phys. Rev. A **45**, 8185 (1992).
2. M. Aspelmeyer, T. J. Kippenberg, and F. Marquardt, Rev. Mod. Phys. **86**, 1391 (2014).
3. M. Padgett and R. Bowman, Nat. Photonics **5**, 343 (2011).
4. J. Wang, J.-Y. Yang, I. M. Fazal, N. Ahmed, Y. Yan, H. Huang, Y. Ren, Y. Yue, S. Dolinar, M. Tur, and A. E. Willner, Nat. Photonics **6**, 488 (2012).
5. G. Molina-Terriza, J. P. Torres, and L. Torner, Nat. Phys. **3**, 305 (2007).
6. M. Erhard, R. Fickler, M. Krenn, and A. Zeilinger, Light Sci. Appl. **7**, 17146 (2018).
7. K. Dholakia, N. B. Simpson, M. J. Padgett, and L. Allen, Phys. Rev. A **54**, R3742 (1996).
8. F. Kong, C. Zhang, F. Bouchard, Z. Li, G. G. Brown, D. H. Ko, T. J. Hammond, L. Arissian, R. W. Boyd, E. Karimi, and P. B. Corkum, Nat. Commun. **8**, 14970 (2017).
9. A. Mair, A. Vaziri, G. Weihs, and A. Zeilinger, Nature **412**, 313 (2001).
10. J. Wang, J. Liu, S. Li, C. Klitis, M. Sorel, S. Yu, and X. Cai, in *Conference on Lasers and Electro-Optics Pacific Rim (CLEO-PR)* (IEEE, 2017), pp. 1–2.
11. H. Li, D. B. Phillips, X. Wang, Y.-L. D. Ho, L. Chen, X. Zhou, J. Zhu, S. Yu, and X. Cai, Optica **2**, 547 (2015).
12. N. Carlon Zambon, P. St-Jean, M. Milićević, A. Lemaître, A. Harouri, L. Le Gratiet, O. Bleu, D. D. Solnyshkov, G. Malpuech, I. Sagnes, S. Ravets, A. Amo, and J. Bloch, Nat. Photonics **13**, 283 (2019).
13. A. S. Desyatnikov, Y. S. Kivshar, and L. Torner, Prog. Opt. **47**, 291 (2005).
14. V. Sala, D. Solnyshkov, I. Carusotto, T. Jacqmin, A. Lemaître, H. Terças, A. Nalitov, M. Abbarchi, E. Galopin, I. Sagnes, J. Bloch, G. Malpuech, and A. Amo, Phys. Rev. X **5**, 011034 (2015).
15. S. Dufferwiel, F. Li, E. Cancellieri, L. Giriunas, A. Trichet, D. Whittaker, P. Walker, F. Fras, E. Clarke, J. Smith, M. Skolnick, and D. Krizhanovskii, Phys. Rev. Lett. **115**, 246401 (2015).
16. K. Y. Bliokh, F. J. Rodríguez-Fortuño, F. Nori, and A. V. Zayats, Nat. Photonics **9**, 796 (2015).
17. S. Michaelis de Vasconcellos, A. Calvar, A. Dousse, J. Suffczyński, N. Dupuis, A. Lemaître, I. Sagnes, J. Bloch, P. Voisin, and P. Senellart, Appl. Phys. Lett. **99**, 101103 (2011).
18. H. Ando, T. Sogawa, and H. Gotoh, Appl. Phys. Lett. **73**, 566 (1998).
19. R. Butté, G. Delalleau, A. I. Tartakovskii, M. S. Skolnick, V. N. Astratov, J. J. Baumberg, G. Malpuech, A. Di Carlo, A. V. Kavokin, and J. S. Roberts, Phys. Rev. B **65**, 205310 (2002).
20. C. L. Tang, A. Schremer, and T. Fujita, Appl. Phys. Lett. **51**, 1392 (1987).
21. H. Kawaguchi, I. H. White, M. J. Offside, and J. E. Carroll, Opt. Lett. **17**, 130 (1992).
22. H. Kawaguchi, IEEE J. Sel. Top. Quantum Electron. **3**, 1254 (1997).